Journal of Nondestructive Evaluation (2024) 43:51
https://doi.org/10.1007/s10921-024-01078-5

# Reconstruction of Metal Defect Images Based on the Sensitivity Matrix of High Conductivity Initial Estimate for Eddy Current Tomography

Zhili Xiao[1] · Zicheng Ma[1] · Xiaohui Li[1] · Chao Tan[2] · Feng Dong[2]

Received: 31 December 2023 / Accepted: 2 April 2024 / Published online: 25 April 2024
© The Author(s), under exclusive licence to Springer Science+Business Media, LLC, part of Springer Nature 2024

**Abstract**
Eddy current testing is one of the conventional non-destructive testing (NDT) technologies which is widely used in metal defects detection. Defect imaging by eddy current tomography (ECT) has advantages of visualization of defects, large detection area, fast detection speed and avoiding mechanical scanning imaging error. Sensitivity matrix is crucial in reconstructing defect images of metal materials by ECT. This article presents a sensitivity matrix of high conductivity initial estimate for ECT detecting metal materials. A 4×4 eddy current planar coil array and a 2 mm thickness titanium plate with defects were designed by both simulation and experiment. Based on the proposed sensitivity matrix, reliability of ECT forward problem linearization was analyzed and image reconstruction with two typical regularization methods ($L_1$ and $L_2$) were investigated. Both simulation and experiment results show that ECT forward problem linearization was more accurate and reliable with the proposed sensitivity matrix especially at higher frequency. And $L_1$ regularization method was verified to be more suitable to reconstruct image of small defects in metal materials. This work expands the original assumption of ECT forward problem linearization, which is of great significance to improve the metal defect image accuracy of ECT.

**Keywords** Eddy current tomography · Defects · Imaging · Reconstruction · Sensitivity matrix

## 1 Introduction

Various harsh environments are encountered during the manufacturing and service of the aeroengine blades, such as high temperature, high pressure, and high speed. Crack defects usually appear on the blades, which seriously threat to aircraft flight safety [1]. Nondestructive testing (NDT) technology can detect, locate and image the fatigue and corrosion cracks without damaging the tested object, which is widely used in many areas including aeronautics and astronautics, industry, and so on [2, 3]. Eddy current testing of NDT can detect the surface and near surface defects of aircraft engine blades due to the advantages of non-contact and high sensitivity [4, 5]. The electromagnetic characteristics and material discontinuities of the tested object can be judged according to the signal change of sensing sensor caused by eddy current in the tested object.

Eddy current imaging can be used to characterize the defect visually. There are two kinds of imaging methods. One is scanning imaging, and the pixels in the image represent the detection signal amplitude or phase of the sensing sensor. The images are obtained by mechanical scanning of the tested object through a single sensor or linear array sensing sensors [6–8]. The copper islands on printed circuit board was imaged by a scanning system comprised by an array of two coils [9, 10]. Another ECT setup with two air-core co-axial coils located between a cylindrical sample along with rotary actuator and linear actuator was studied [11]. These works are all mechanical scanning required. Mechanical scanning

✉ Zhili Xiao
zlxiao@cauc.edu.cn

Zicheng Ma
mayuepeng@163.com

Xiaohui Li
1139076432@qq.com

Chao Tan
tanchao@tju.edu.cn

Feng Dong
fdong@tju.edu.cn

[1] College of Electronic Information and Automation, Civil Aviation University of China, Tianjin 300300, China

[2] Tianjin Key Laboratory of Process Measurement and Control, School of Electrical and Information Engineering, Tianjin University, Tianjin 300300, China

will cause errors in the detection results, especially for the curved parts such as aircraft engine blades [12].

The other imaging method is image reconstruction, and the pixels in the image represent the conductivity distribution of the tested object [13]. This imaging method is also known as eddy current tomography (ECT), magnetic induction tomography (MIT) and electromagnetic tomography (EMT) [14]. ECT with multi sensor eddy current array can obtain large detection area, improve detection speed and avoid mechanical scanning error [15, 16]. Since sensor number is limited, the number of detection signals is far less than the unknown conductivity distribution, which leads to the serious ill condition of the inverse problem. Regularization is usually introduced to solve the inverse problem based on sensitivity matrix [9]. The spectral imaging was studied by using adaptive spectral correlation basis algorithm with 8-coil ring array [17]. An inverse solver based on the Gauss-Newton-one-step method was investigated with four different regularization schemes for differential image reconstruction of a spherical perturbation within a conducting cylinder [18]. A nonlinear, iterative inverse solver based on regularized Gauss-Newton algorithm was studied for reconstructing absolute conductivity distribution images by a cylindrical 8-coil array [19]. The Tikhonov regularization method has been widely used in the ill-conditioned inverse problem. Frequency-difference images of cerebral haemorrhage were reconstructed by Tikhonov regularization with a cylindrical coil array and a hemispherical coil array [20]. The conductivity distribution of aluminium rods was calculated by standard Tikhonov regularization method with a planar 16-coil array at 50 kHz [21]. The conductivity inhomogeneity on a metal plate was detected by a planar 8-coil array at 10 kHz [22]. The sensitivity matrix in these works was based on the unit conductivity initial estimate (1 S/m ) throughout the region of interest (ROI) [20, 23–25]. Since the conductivity of the aeroengine blades is large which leads to serious skin effect at high frequency, the initial estimate of conducting distribution for computing the sensitivity matrix is of some importance [26].

This paper aims to study metal defects detection by ECT based on the sensitivity matrix of high conductivity initial estimate. Both simulation and experiment are conducted to examine the influence of unit conductivity and high conductivity initial estimate sensitivity matrix on the reliability of forward problem linearization. And the imaging performance of $L_1$ and $L_2$ regularization methods are then compared to reconstruct metal defects based on high conductivity initial estimate sensitivity matrix at different frequencies. The simulation and experimental results show that proposed method improves the metal defect image accuracy of ECT.

## 2 Theory

ECT is based on Maxwell's electromagnetic field theory and can be divided into forward problem and inverse problem [27].

### 2.1 Forward Problem Linearization

The forward problem quantitatively analyzes the magnetic field, impedance changes, or induced voltage with given excitation current and a particular type of defect in a particular location. The forward problem is non-linear which can be expressed as [26]:

$$\mathbf{V} = F(\sigma) \tag{1}$$

where $\sigma$ represents true conductivity distribution of the tested object, $\mathbf{V}$ stands for the induced voltages of all excitation-detection configurations, and $F$ is a non-linear function of the forward problem.

Assuming that there is a small conductivity perturbation between the two states of the tested object, the forward problem can be approximated by applying truncated Taylor series and ignoring the small second and higher order terms. This process is called forward problem linearization [26, 28].

$$\Delta\mathbf{V} = F(\sigma) - F(\sigma_0) \approx \left.\frac{\partial F}{\partial \sigma}\right|_{\sigma_0} (\sigma - \sigma_0) = \mathbf{S}\Delta\sigma \tag{2}$$

where $\Delta\mathbf{V}$ is the voltage changes; $\Delta\sigma$ is the conductivity changes; $\partial F/\partial\sigma$ is the Jacobian matrix computed at certain initial conductivity estimate $\sigma_0$, which is the same with sensitivity matrix $\mathbf{S}$; $\mathbf{S}$ maps the sensitivity of a small conductivity perturbation $\Delta\sigma$ of specific voxel to voltage changes of $m$ excitation-detection configurations.

### 2.2 Sensitivity Matrix

The mutual impedance changes $\Delta Z$ for an excitation-detection configuration of coil 1 (c1) and coil 2 (c2) can be derived in terms of the corresponding magnetic and electric fields based on Lorentz reciprocity theorem [27, 29] as :

$$\begin{aligned}\Delta Z = Z_b - Z_a = \frac{1}{I^2}\int_v \mathrm{j}\omega(\mu_b - \mu_a)\mathbf{H}_{c1}^a \cdot \mathbf{H}_{c2}^b \\ -(\sigma_b + \mathrm{j}\omega\varepsilon_b - \sigma_a - \mathrm{j}\omega\varepsilon_a)\mathbf{E}_{c1}^a \cdot \mathbf{E}_{c2}^b dv\end{aligned} \tag{3}$$

where $Z_a$ is the mutual impedance between c1 and c2 when the tested object properties are $\mu_a$ (permeability), $\varepsilon_a$ (permittivity), $\sigma_a$ and an alternating current $I$, of angular frequency $\omega$, is applied to coil c1 to produce the magnetic field $\mathbf{H}_{c1}^a$ and electric field $\mathbf{E}_{c1}^a$; $Z_b$ is the mutual impedance for the tested object properties are $\mu_b$, $\varepsilon_b$, $\sigma_b$ and fields are $\mathbf{H}_{c2}^b$, $\mathbf{E}_{c2}^b$

produced by the same current and frequency injecting into c2. The volume of integration $v$ should include the regions where the tested object properties are changed.

For ECT detecting defects of the non-ferromagnetic high conductivity aeroengine blades, $\mu$ and $\varepsilon$ of the material are the same with the air and the defects are detected by measuring the changes with respect to the initial conductivity estimate $\sigma_0$. Therefore, $\Delta Z$ can be simplified with $\sigma_a$ replaced by $\sigma_0$ as:

$$\Delta Z \approx -\frac{1}{I^2}\int_v (\sigma_b - \sigma_0)\mathbf{E}_{c1}^0 \cdot \mathbf{E}_{c2}^b dv = -\frac{\Delta\sigma}{I^2}\int_v \mathbf{E}_{c1}^0 \cdot \mathbf{E}_{c2}^b dv \tag{4}$$

Then voltage changes in the detection coil is

$$\Delta V = I\Delta Z \approx -\frac{\Delta\sigma}{I}\int_v \mathbf{E}_{c1}^0 \cdot \mathbf{E}_{c2}^b dv \tag{5}$$

Note that $\mathbf{E}_{c1}^0$ and $\mathbf{E}_{c2}^b$ are the electric field caused by different conductivity distribution ($\sigma_0$ and $\sigma_b$) with different coil excited (c1 and c2).

By discretizing the volume of integration $v$ into $n$ homogeneous voxels, the voltage changes $\Delta V$ can be expressed by:

$$\Delta V = \sum_{i=1}^{n}\Delta V_i = -\frac{1}{I}\sum_{i=1}^{n}\left(\Delta\sigma_i \mathbf{E}_{c1}^0|_i \cdot \mathbf{E}_{c2}^b|_i \Delta v\right) \tag{6}$$

where $\Delta v$ is the volume of the discrete voxel.

When $\sigma_b$ and $\sigma_0$ are the same, $\partial F/\partial\sigma$ at $\sigma_0$ can be expressed as:

$$\left.\frac{\partial F}{\partial\sigma}\right|_{\sigma_0} = S_{k,i} = \lim_{\Delta\sigma_i\to 0}\frac{\Delta V_i}{\Delta\sigma_i} = -\frac{1}{I}\mathbf{E}_{c1}^0|_i \cdot \mathbf{E}_{c2}^0|_i \Delta v \tag{7}$$

where $\mathbf{E}_{c1}^0|_i$ is the electric field at voxel $i$ caused by the same initial conductivity estimate $\sigma_0$ to $\mathbf{E}_{c2}^0|_i$, and these electric field values are generally obtained by simulation; $S_{k,i}$ is an element of $\mathbf{S}_{m\times n}$.

It is worth noting that $S_{k,i}$ not only depends on the electrical properties of the material within the voxel but from all the distribution in the sensing area since the surrounding area affects the current flow in the voxel [29]. Moreover, the skin-effect of electromagnetic wave is closely related to frequency and conductivity which limits the detection depth on highly conductive metal materials. Therefore, the conductivity of the tested object and the excitation frequency should both be considered while making the choice of the initial conductivity estimate $\sigma_0$ .

#### 2.2.1 Unit Conductivity Initial Estimate

In the condition that skin depth of the electromagnetic wave in the tested object is larger than the dimensions of the sample (also known as "weak skin effect"), the amplitude response $\Delta V$ is proportional to the conductivity and the square of the frequency, i.e. $\Delta V \propto \sigma f^2$ [30, 31]. In our previous work, this specific relationship is verified to be valid only below a specified frequency (upper limit frequency) when ECT inspects the defects of high conductivity metal materials. For a 2 mm thickness titanium plate ($\sigma = 7.407 \times 10^5$ S/m), the upper limit frequency is 2kHz in weak skin effect condition [32].

In image reconstruction of low conductivity biological tissue detection by MIT, unit conductivity initial estimate is always used to calculate the sensitivity matrix [24, 28, 31]. In the weak skin effect condition for ECT detecting high conductivity metal materials, $\Delta V \propto \sigma f^2$, so $\partial F/\partial\sigma$ is constant at a certain frequency. That is to say the element $S_{k,i}$ of sensitivity matrix has nothing to do with the value of initial conductivity estimate $\sigma_0$. The unit conductivity initial estimate is still available below the upper limit frequency.

#### 2.2.2 High Conductivity Initial Estimate

When the frequency is higher than the upper limit frequency, the skin effect is relatively serious and the conditions for weak skin effect are no longer satisfied. The relationship between the amplitude response $\Delta V$ and the conductivity $\sigma$ changes and becomes non-linear, which means $\partial F/\partial\sigma$ is different with different initial conductivity estimate $\sigma_0$ at a certain higher frequency. That is to say the unit conductivity initial estimate is no longer available to calculate the sensitivity matrix.

The tested object discussed is solid metal aeroengine blade with fixed shape, which is homogeneous, high conductivity, and non-ferromagnetic. Defects can be seen as high conductivity perturbation on initial defect free tested object which is unsatisfied the assumption of a small conductivity perturbation in equation 2. However, the non-destructive testing on aeroengine blade by ECT is intended to detect small defects, such as cracks, which can be considered as small volume perturbation on initial defect free blade. Therefore, the high conductivity initial estimate $\sigma_0$ is proposed to calculate the sensitivity matrix at the frequency higher than the upper limit frequency and $\sigma_0$ is same to the conductivity of the tested object based on equation 2.

### 2.3 Image Reconstruction

The aim of ECT inverse problem is to reconstruct the conductivity distribution changes from detection changes which is also known as image reconstruction. Two typical $L_1$ and $L_2$

regularization reconstruction algorithms [33] are discussed and compared in the metal defect imaging by ECT.

#### 2.3.1 $L_2$ Regularization Method

$L_2$ regularization is known as $L_2$-regularized least squares, Tikhonov regularization or Ridge Regression problem, which is described as [34]:

$$\Delta\hat{\sigma} = \arg\min_{\Delta\sigma} ||\Delta\mathbf{V} - \mathbf{S}\Delta\sigma||_2^2 + \lambda_2||\Delta\sigma||_2^2 \tag{8}$$

where $||\cdot||_2$ refers to the $L_2$ norm of a vector; $\lambda_2$ is the $L_2$ regularization parameter. The optimal solution is easy to obtained since the penalty term $\lambda_2||\Delta\sigma||_2^2$ is differentiable.

$$\Delta\hat{\sigma} = \left(\mathbf{S}^T\mathbf{S} + \lambda_2\mathbf{I}\right)^{-1}\mathbf{S}^T\Delta\mathbf{V} \tag{9}$$

$L_2$ regularization method is good at solving the least square optimization problem based on the prior knowledge that the difference of $\Delta\sigma$ element is small.

#### 2.3.2 $L_1$ Regularization Method

$L_1$ regularization is known as $L_1$-regularized least squares or LASSO (Least absolute shrinkage and selection operator) problem, which is described as [34]:

$$\Delta\hat{\sigma} = \arg\min_{\Delta\sigma} ||\Delta\mathbf{V} - \mathbf{S}\Delta\sigma||_2^2 + \lambda_1||\Delta\sigma||_1 \tag{10}$$

where $\lambda_1$ is the $L_1$ regularization parameter. The optimal solution is more difficult to be calculated than $L_2$ regularization because the penalty term $\lambda_1||\Delta\sigma||_1$ is non-differentiable at $\Delta\sigma = 0$.

Proximal Gradient Method (PGM) is a special gradient descent method, which is mainly used to solve the optimization problems with non-differentiable objective functions. The iterative shrinkage threshold algorithm (ISTA) belongs to PGM for LASSO problem which is implemented to solve equation 10. The priori knowledge of L1 regularization method is fewer non-zero reconstructing elements which is different from $L_2$ regularization method.

## 3 Material and Methods

### 3.1 Numerical Modeling of ECT Coil Array

The forward problem of ECT is solved by finite-element (FE) software COMSOL and then the voltages on the detection coils are obtained.

The aeroengine turbine blades are solid metal with curved shapes. In the preliminary basic theoretical research of this paper, the curved blade is simplified into a 200 mm×200 mm×2 mm titanium planar plate. A 4×4 eddy current planar coil array and defect models with different positions are established as shown in Fig. 1. The coil wire is selected as No.26 American wire gauge (AWG) according to the amplitude of excitation. The parameters for all coils are the same (shown in Table 1) which can either be excitation coil or detection coil. The excitation strategy is each single coil excited by a 0.4 A sinusoidal current of different frequencies circularly, and the other coils are used for detection. A total of 240 (16×15) detection voltages for all excitation-detection configurations are obtained for image reconstruction. Surface defect models with different positions, dimensions (length, width and depth), and orientations are shown in Table 2.

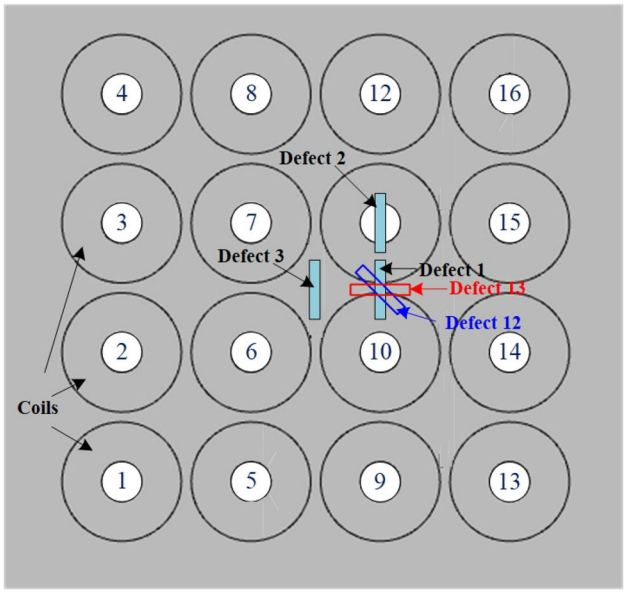


**Fig. 1** Planar ECT array with different defects

### 3.2 Experimental Setup

A 4×4 eddy current planar coil array is designed for experiment which is the same to the simulation model. The coils are wound by enameled copper wire whose coil parameters in experiment are also shown in Table 1. The turns of the experimental coils are a little less than the simulation due to the tightness influence of manual coil winding. The spacing between adjacent coils is 1 mm which is the same to simulation. A 200 mm×200 mm×2 mm titanium planar plate with a 10 mm×1 mm×2 mm defect is detected and reconstructed by the planar coil array. And the titanium planar plate without defect is employed as the reference. Fig. 2 shows the experimental planar coil array and tested titanium planar plate.

The impedances of 16 coils are measured by the impedance analyzer. Figure 3 shows the average impedances and max

**Table 1** Coil parameters for planar array of ECT

| Parameters | Simulation values | Experimental values |
|---|---|---|
| Internal diameter (mm) | 4 | 4 |
| External diameter (mm) | 12 | 12 |
| Height (mm) | 8 | 8 |
| No. of turns | 153 | 146 |
| Wire diameter (mm) | 0.405 | 0.41 |
| Inductance ($\mu$H) | 84.5 | 85.2± 0.65 |

**Table 2** The number, dimension and type of defects (Unit:mm)

| Defect no | Length×width×depth | Coordinate | Defect type |
|---|---|---|---|
| Defect 1 | 6×1×1 | (6.5,0,0.5) | defect position |
| Defect 2 | 6×1×1 | (6.5,6.5,0.5) | |
| Defect 3 | 6×1×1 | (0,0,0.5) | |
| Defect 4 | 6×1×0.5 | (6.5,0,0.75) | defect depth |
| Defect 5 | 6×1×0.2 | (6.5,0,0.9) | |
| Defect 6 | 4×1×1 | (6.5,0,0.5) | defect length |
| Defect 7 | 2×1×1 | (6.5,0,0.5) | |
| Defect 8 | 6×0.5×1 | (6.5,0,0.5) | defect width |
| Defect 9 | 6×2×1 | (6.5,0,0.5) | |
| Defect 10 | 6×4×1 | (6.5,0,0.5) | |
| Defect 11 | 6×6×1 | (6.5,0,0.5) | |
| Defect 12 | 6×1×1 (45°) | (6.5,0,0.5) | defect orientation |
| Defect 13 | 6×1×1 (90°) | (6.5,0,0.5) | |
| Defect 14 | 6×1×1 (135°) | (6.5,0,0.5) | |

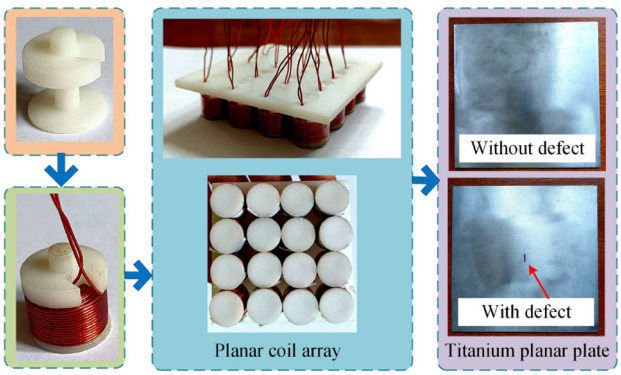


**Fig. 2** Experimental planar coil array and tested titanium planar plate

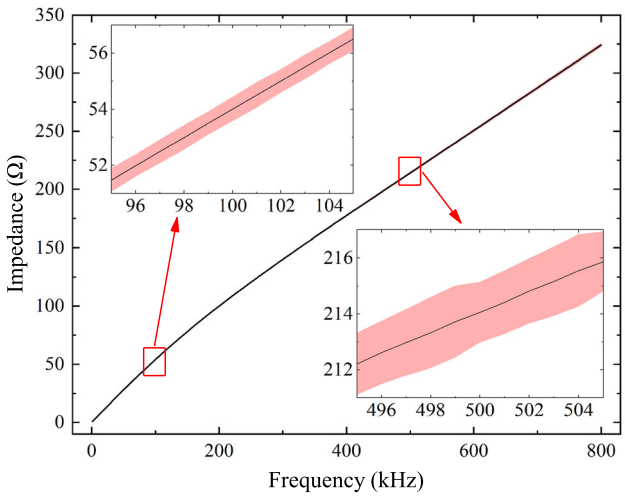


**Fig. 3** Average impedance spectrum and max absolute errors of all coils in experiment

absolute error of all coils from 1 kHz to 800 kHz. Two frequencies of 100 kHz and 500 kHz are employed in the experiment. The average impedances of all coils at 100 kHz and 500 kHz are 54 Ω and 214 Ω, respectively. And the max relative errors are 0.8% and 0.5%, which indicates the high consistency of all coils.

The experimental platform is shown in Fig. 4. The voltage signal generated by the signal generator is amplified by a power amplifier to excite the coil. The coil impedance is too small at lower frequencies to meet the requirements of the power amplifier. And when the frequency is high, the coil impedance is large and a larger excitation voltage is required which is also limited by the power amplifier. Therefore, two kinds of sinusoidal voltages with 44 $V_{pp}$, 100 kHz and 58 $V_{pp}$, 500 kHz are used in the experiment. And the excitation currents are 0.81 A and 0.27 A respectively at 100 kHz and 500 kHz. The induced voltages on the detection coils are

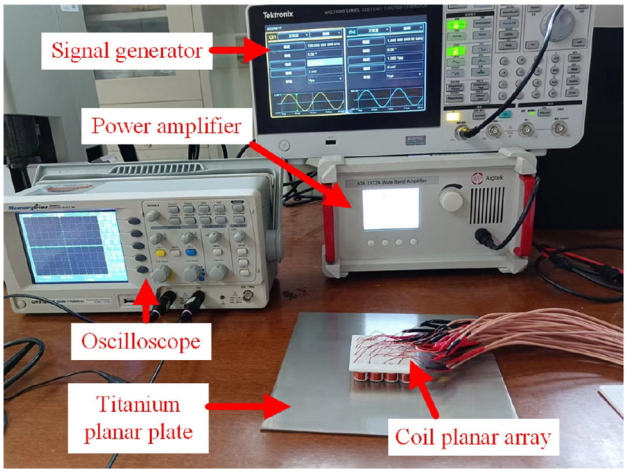


**Fig. 4** Eddy current planar coil array experimental platform

detected and recorded by the oscilloscope. The experiment is conducted with defects at different positions (same to defect 1, 2 and 3 in simulation) which named as defect 1', 2' and 3'.

### 3.3 Forward Problem Linearization Analysis Based on Sensitivity Matrix

Since the accuracy of forward problem linearization affects the performance of image reconstruction directly, the reliability of ECT forward problem linearization based on the sensitivity matrix is examined with unit conductivity and high conductivity initial estimate, respectively.

These two kinds of sensitivity matrices are calculated according to equation 7. The electric fields $\mathbf{E}_{c1}^{0}|_i$ and $\mathbf{E}_{c2}^{0}|_i$ at the central coordinates of all discrete voxels are obtained by setting 1 S/m and $7.407 \times 10^5$ S/m throughout ROI with planar ECT array model in simulation. As the skin effect is more serious with the increase of frequency, 16 layers sensitivity matrices for the ROI of 2 mm thickness planar plate are considered. The inverse problem meshes are voxels of 0.5 mm×0.5 mm×0.125 mm. Moreover, the number of inverse problem meshes directly affect the underdetermined, ill-posedness and computing time of inverse problem. Therefore, 16 layers sensitivity matrices are superposed to become a single layer sensitivity matrix which is used for image reconstruction. The sensitivity maps are characterized by the superposition of all rows of the sensitivity matrix $\mathbf{S}_{m\times n}$.

The reference voltages $\mathbf{V}_0$ and the total voltages $\mathbf{V}$ were recorded when detecting the titanium planar plate without and with defects for all excitation-detection configurations, respectively. Then the voltage changes $\Delta\mathbf{V}$ can be obtained by subtracting $\mathbf{V}_0$ from $\mathbf{V}$.

The reliability of ECT forward problem linearization is quantified by the similarity between voltage changes $\Delta\mathbf{V}$ and $\mathbf{S}\Delta\sigma$. The relative error $\mathrm{RE}_{linear}$ and correlation coefficient $\mathrm{CC}_{linear}$ between the normalization results of voltage changes $\Delta\mathbf{V}$ and $\mathbf{S}\Delta\sigma_{tr}$ are calculated at different frequencies from 1 kHz to 800 kHz.

$$\mathrm{RE}_{linear} = \frac{||N(\Delta\mathbf{V}) - N(\mathbf{S}\Delta\sigma_{tr})||_2}{||N(\mathbf{S}\Delta\sigma_{tr})||_2} \tag{11}$$

$$\mathrm{CC}_{linear} = corr(\Delta\mathbf{V}, \mathbf{S}\Delta\sigma_{tr}) \tag{12}$$

where $\Delta\sigma_{tr}$ is the true conductivity change ($\sigma - \sigma_0$) caused by defect while solving the forward problem to obtain $\Delta\mathbf{V}$; N(·) means the normalization result after scaling between 0 and 1; corr(·, ·) stands for the Pearson product-moment correlation coefficient.

### 3.4 Image Reconstruction of ECT

$L_1$ and $L_2$ regularization methods are compared to reconstruct the image of conductivity change $\Delta\hat{\sigma}$ of the tested object. The regularization parameters of $L_1$ and $L_2$ are selected based on experience by combining the following optimal imaging indicators ($\lambda_1 = 0.01$ and $\lambda_2 = 0.06$). The performance of these two basic regularization methods are compared based on the same sensitivity matrix with different initial conductivity estimates at different frequencies.

The quality of the reconstructed image was assessed by imaging indicators such as correlation coefficient $\mathrm{CC}_{imag}$, relative error $\mathrm{RE}_{imag}$, and localization error $\mathrm{LE}_{imag}$ between the normalization results of reconstructed and true conductivity change. The area P corresponding to the reconstructed defect was identified as the largest connected cluster of meshes with values larger than 50% of the maximum of the image [24].

$$\mathrm{CC}_{imag} = corr(\Delta\hat{\sigma}, \Delta\sigma_{tr}) \tag{13}$$

$$\mathrm{RE}_{imag} = \frac{||N(\Delta\hat{\sigma}) - N(\Delta\sigma_{tr})||_2}{||N(\Delta\sigma_{tr})||_2} \tag{14}$$

$$\mathrm{LE}_{\mathrm{imag}} = ||(\mathrm{x_P}, \mathrm{y_P})||_2 \tag{15}$$

where $(\mathrm{x_P}, \mathrm{y_P})$ is the displacement of the center of mass of the reconstructed defect P from the actual defect location.

## 4 Simulation Results and Discussion

### 4.1 Sensitivity Maps With Different Initial Conductivity Estimates

In order to verify the influence of skin effect on sensitivity matrices, the maximum values for sensitivity matrices of all 16 layers with different initial conductivity estimate at different frequencies are shown in Fig. 5. The horizontal axis

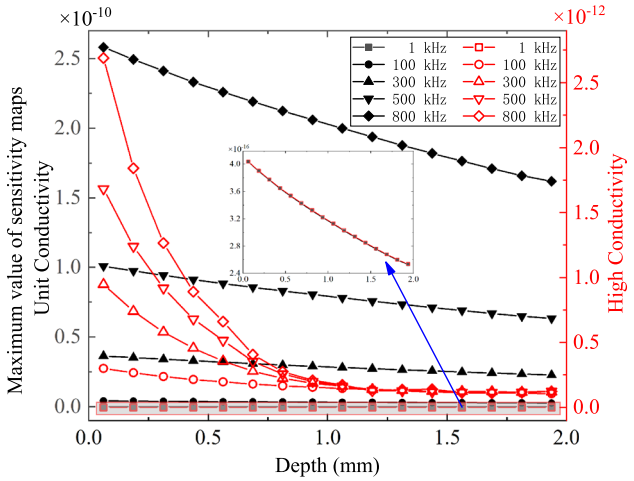


**Fig. 5** Maximum value of sensitivity matrix in each layer with different initial conductivity estimate at different frequencies

represents the depth of sensitivity matrix layer to the surface of the tested plate near the coil array. The left and right ordinates represent the maximum value of each sensitivity matrix layer with unit conductivity and high conductivity initial estimate respectively.

As can be seen, the maximum values for sensitivity matrices of all 16 layers increase with frequency both for unit conductivity and high conductivity initial estimate. For unit conductivity initial estimate, the maximum value decreases slowly with increasing depth at a higher frequency. But for high conductivity initial estimate, the maximum value declines greatly with depth increases due to the increasing skin effect at higher frequency. This indicates that the initial conductivity estimate has great influence on the sensitivity at higher frequency.

The maximum values of sensitivity matrix with different initial conductivity estimate at 1 kHz are enlarged in Fig. 5. They are almost identical which indicates that the initial conductivity estimate has no effect on the sensitivity below the upper limit frequency.

The single layer sensitivity maps with different initial conductivity estimate at different frequencies are shown in Fig. 6. The coils are also plotted. The color bar from blue to red indicates lower sensitivity to higher sensitivity. Because the magnetic field seriously decays with the increasing distance from the coil, only the region near the coil array has high sensitivity.

The sensitivity distributions of sensitivity matrices are similar for the unit conductivity initial estimate at all frequencies and the high conductivity initial estimate at 1 kHz. The sensitivity near the center 4 coils is much higher than that near the outer 12 coils. The maximum sensitivity is obtained between two adjacent coils of the four central coils. And the center of all coils exhibits a low sensitivity characteristic.

For the sensitivity matrix calculated with high conductivity initial estimate, with the increase of frequency, the sensitivity in the region between two adjacent coils is obviously strengthened and the sensitivity in other regions is relatively weaken.

## 4.2 Forward Problem Linearization Analysis Based on Sensitivity Matrix

In order to examine the reliability of ECT forward problem linearization based on the sensitivity matrix with two kinds of initial conductivity estimates, the relative error $RE_{linear}$ and the correlation coefficient $CC_{linear}$ are shown in Fig. 7. Three kinds of defects (defect 1–3) with the same dimension at different locations relative to the coil array are involved and frequencies of 1 kHz, 100 kHz, 300 kHz, 500 kHz, and 800 kHz are included.

$RE_{linear}$ and $CC_{linear}$ are almost the same at 1 kHz for the sensitivity matrix calculated with unit conductivity and high conductivity initial estimates. With frequency increases, $RE_{linear}$ and $CC_{linear}$ for unit conductivity initial estimate are larger and smaller than high conductivity initial estimate, respectively. This indicates that the ECT forward problem linearization is more accurate and more reliable for the sensitivity matrix calculated with high conductivity initial estimate at hundreds of kHz.

What's more, for the three defects at different positions, the indicators for defect 1 locating at the center of two adjacent coils of the four central coils are the best where $RE_{linear}$ is 1.76% and $CC_{linear}$ is 0.9999 at 500 kHz. And this best detection location is in agreement with the sensitivity maps shown Fig. 6.

The influence of defect dimension (depth, length, width) on the performance of the ECT forward problem linearization is carried out. The high conductivity initial estimate sensitivity matrix at 500 kHz is adopted and the defects are at the best detection location.

As shown in Fig. 8(a), $RE_{linear}$ reduces and $CC_{linear}$ increases with the depth of surface defect decreases. When the defect depth is 0.2 mm, $RE_{linear}$ reduces to 0.66% and $CC_{linear}$ increases to 1. Similar changes are shown in Fig. 8(b) for different length of defects. With the length of defect decreases, $RE_{linear}$ reduces and $CC_{linear}$ increases. For the defect length of 2 mm, $RE_{linear}$ is 0.8% and $CC_{linear}$ is 1. Figure 8(c) shows the best forward problem linearization indicators of $RE_{linear}$ and $CC_{linear}$ appear at defect width of 4 mm. For all these defects with different dimensions, $RE_{linear}$ retains below 2% and $CC_{linear}$ retains above 0.9998, which show good reliability of ECT forward problem linearization based on high conductivity initial estimate sensitivity matrix at higher frequency.

In the forward problem linearization theory, assumption of a small conductivity change between the defect state and non-

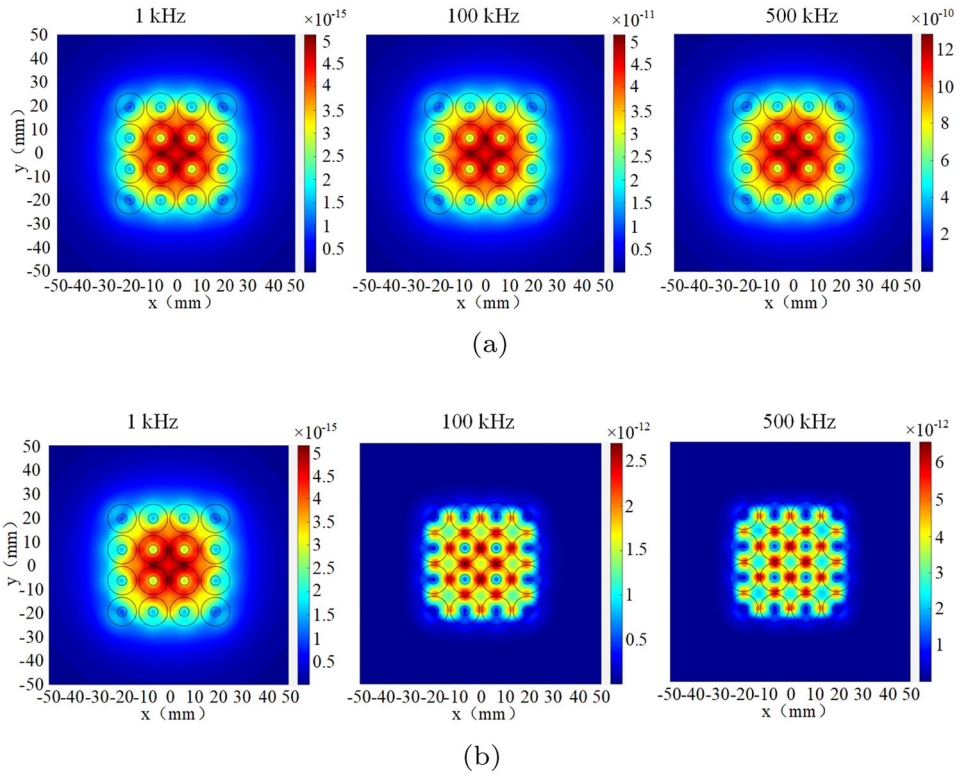


**Fig. 6** Sensitivity maps with different initial conductivity estimate at different frequencies. **a** Unit conductivity initial estimate. **b** High conductivity initial estimate

defect state is adopted. However, the discussed air occupying defect with a conductivity change of $7.407 \times 10^5$ S/m obviously does not meet this assumed premise. According to the influence analysis of defect dimension on the ECT forward problem linearization, smaller dimension of defect expects a better linearization of ECT forward problem. Therefore, a high conductivity change with a small volume perturbation between the defect state and non-defect state can also be applicable for the assumption of forward problem linearization.

### 4.3 Image Reconstruction

The high conductivity initial estimate sensitivity matrix is used to reconstruct the defects by $L_1$ and $L_2$ regularization methods, respectively. Figure 9 shows the reconstructed images of defects with different positions at 1 kHz and 500 kHz. For better comparison, all the images are normalized. The positions of defect 1 and 2 are both well reconstructed at 1 kHz and 500 kHz. And the reconstructed images of defect 3 is significantly better at 500 kHz than 1 kHz. Table 3 shows the imaging parameters of quantitative analysis. $CC_{imag}$ and $RE_{imag}$ of defect 1 and 2 at 500 kHz is slightly better than 1 kHz, but the localization error $LE_{imag}$ at 500 kHz is much smaller than 1 kHz. Especially for the defect 1 with $L_1$ regularization method, the $LE_{imag}$ is 0.01mm at 500 kHz. This indicates that image reconstruction at higher frequency of 500 kHz gets better results than lower frequency of 1 kHz.

The imaging performance of $L_1$ and $L_2$ regularization methods is then compared at 500 kHz. The positions of defect 1, 2, 3 are well located by both two imaging methods. Table 3 shows that $RE_{imag}$ and $LE_{imag}$ of $L_1$ regularization method are obviously better than $L_2$ regularization method. The size of the defects reconstructed by $L_2$ regularization method is larger than real defects while it is opposite for $L_1$ regularization method. This is probably due to the different priori knowledge of these two regularization methods. For $L_2$ regularization method, the priori knowledge is that the difference in reconstructing element values is small. While for $L_1$ regularization method, the priori knowledge is that the non-zero reconstructing elements are few which is more suitable to reconstruct small defects of metal materials theoretically relative to $L_2$ regularization method. However, the shape of defect 1, 2 and 3 all fails to be reconstructed.

Figure 10 compares the imaging performance of $L_1$ and $L_2$ regularization method at 500 kHz for the defects with minimum dimensions of depth (defect 5), length (defect 7) and width (defect 8). Similarly, the positions of all the defects are well located by both two imaging methods. And the size of the defects reconstructed by $L_2$ regularization method is larger than $L_1$ regularization method.

Figure 11 shows $CC_{imag}$ (left vertical axis) and $RE_{imag}$ (right vertical axis) reconstructed by $L_1$ and $L_2$ regularization method for defect 5, 7 and 8. As can be seen, for all the defects, the $CC_{imag}$ and $RE_{imag}$ of $L_1$ regularization method are better than $L_2$ regularization method. Especially

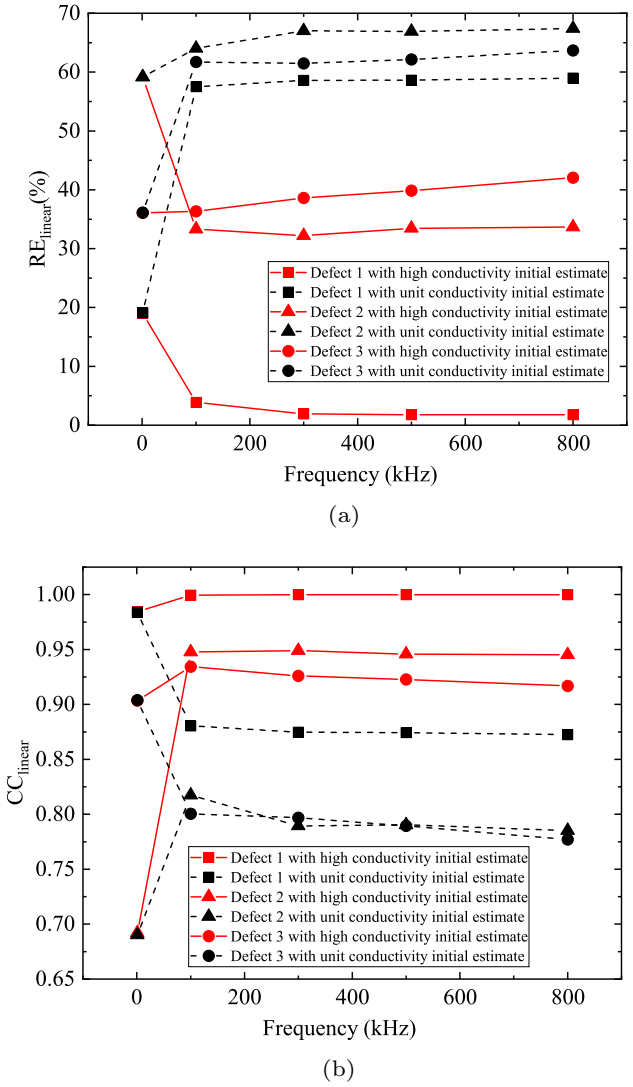


**Fig. 7** Indicators of ECT forward problem linearization based on sensitivity matrices with different initial conductivity estimate at different frequencies for defect 1, 2, and 3. **a** Relative error. **b** Correlation coefficient

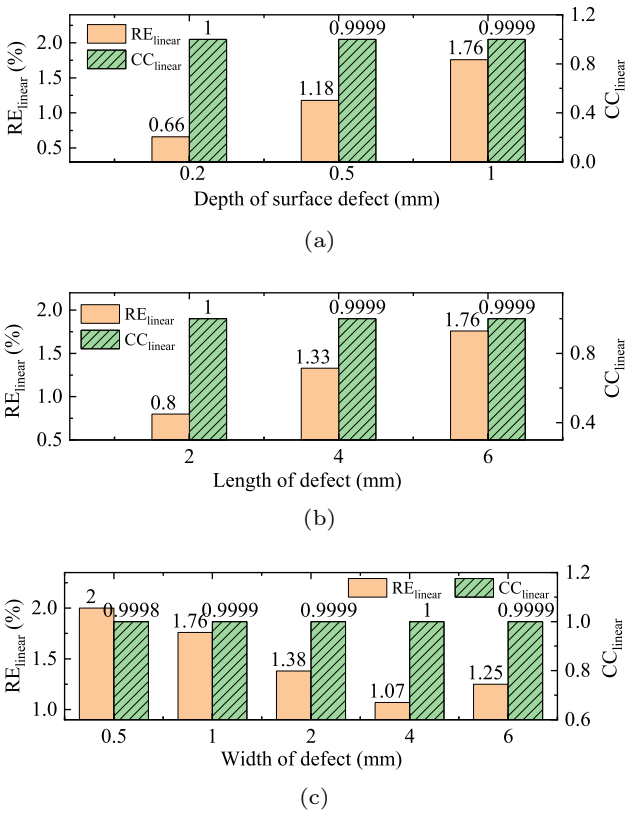


**Fig. 8** Indicators of ECT forward problem linearization based on high conductivity initial estimate sensitivity matrix at 500 kHz. **a** Different depth of surface defect. **b** Different length of surface defect. **c** Different width of surface defect

for the defect 7, $CC_{imag}$ increases from 0.3974 to 0.9096, and $RE_{imag}$ decreases from 224% to 41.6%.

Figure 12 compares the imaging performance of $L_1$ and $L_2$ regularization method at 500 kHz for the defects with different orientations (defect 12, 13 and 14). The shapes of defect 12 (45°) and 14 (135°) are successfully reconstructed by $L_1$ regularization method which is much better than $L_2$ regularization method. For the defect 13, $L_1$ regularization method reconstructs the artifacts in the correct 90° orientation, but the orientation reconstructed by $L_2$ regularization method is totally wrong.

Figure 13 shows the $CC_{imag}$ and $RE_{imag}$ of defect 12, 13 and 14 reconstructed by $L_1$ and $L_2$ regularization method. The $CC_{imag}$ and $RE_{imag}$ of $L_1$ regularization method are much better than $L_2$ regularization method especially for the defect orientations of 45° and 135°. The $CC_{imag}$ increases from 0.5511 to 0.9266, and $RE_{imag}$ decreases from 126.04% to 49.93% for defect 14 (135°) .

## 5 Experimental Results and Discussion

### 5.1 Voltages Comparison Between Simulation and Experiment

The sensitivity matrix is calculated based on an alternating excitation current. The coil impedance varies with frequency. The same excitation voltages at different frequencies can cause different excitation currents. Voltage excitation mode could increase the difficulty of simulation and calculation of the sensitivity matrix. Therefore, current excitation mode is adopted in simulation. However, voltage excitation mode is used in the experiment. The excitation current is calculated by excitation voltages and coil impedance.

Figure 14 compares the reference voltages between simulation and experiment when detecting the titanium planar plate without defects at 100 kHz and 500 kHz. The amplitude of voltages in experiment is larger than simulation at

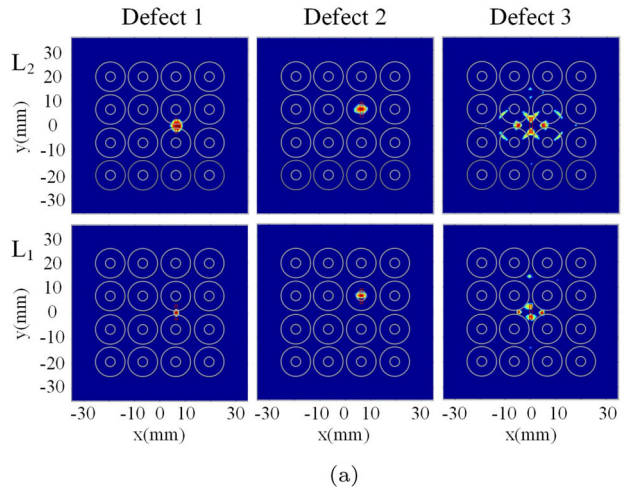


**Fig. 9** Images of defect 1, 2, and 3 reconstructed by $L_1$ and $L_2$ regularization method using high conductivity initial estimate sensitivity matrix. **a** 1 kHz. **b** 500 kHz

**Table 3** The imaging parameters reconstructed by $L_1$ and $L_2$ regularization method at 1 kHz and 500 kHz

| Defect no | Method | Frequency | $CC_{imag}$ | $RE_{imag}$ | $LE_{imag}$ |
|---|---|---|---|---|---|
| Defect 1 | $L_2$ | 1 kHz | 0.50 | 121% | 0.23mm |
| | | 500 kHz | 0.54 | 122% | 0.04mm |
| | $L_1$ | 1 kHz | 0.57 | 83% | 0.10mm |
| | | 500 kHz | 0.53 | 85% | 0.01mm |
| Defect 2 | $L_2$ | 1 kHz | 0.36 | 114% | 0.30mm |
| | | 500 kHz | 0.44 | 112% | 0.07mm |
| | $L_1$ | 1 kHz | 0.36 | 103% | 0.30mm |
| | | 500 kHz | 0.49 | 88% | 0.04mm |

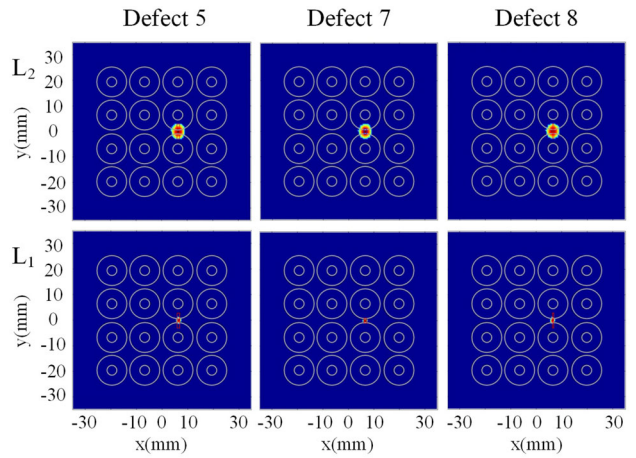


**Fig. 10** Defect images of different dimensions reconstructed by $L_1$ and $L_2$ regularization method at 500 kHz

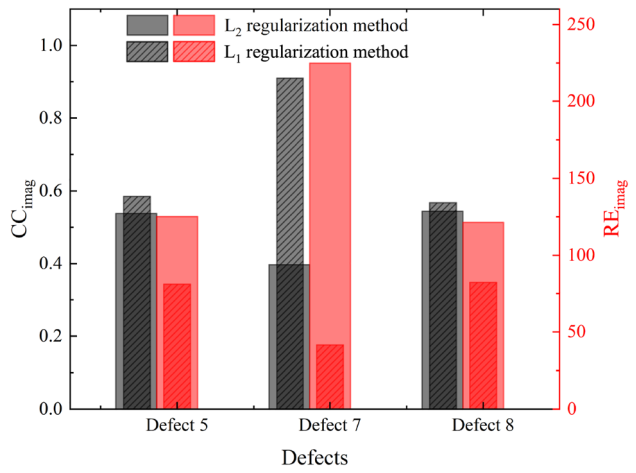


**Fig. 11** $CC_{imag}$ and $RE_{imag}$ of different dimension defects reconstructed by $L_1$ and $L_2$ regularization method

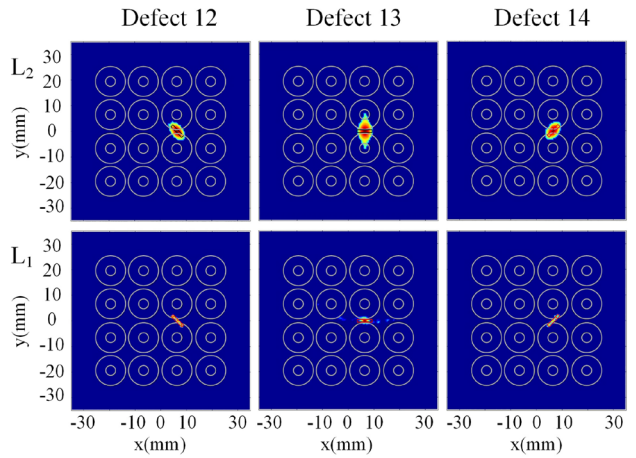


**Fig. 12** Defect images of different orientations reconstructed by $L_1$ and $L_2$ regularization method at 500 kHz

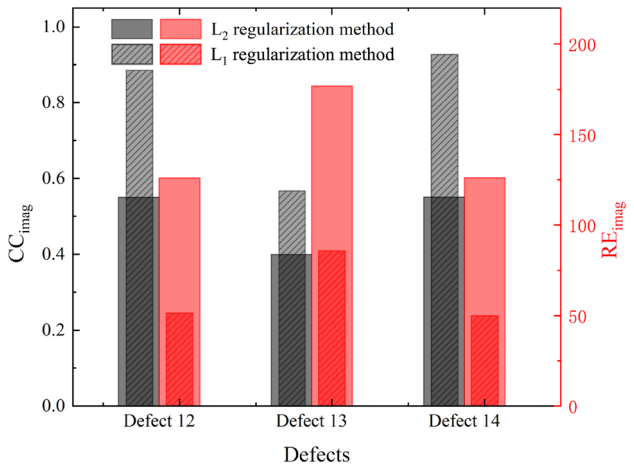


**Fig. 13** $CC_{imag}$ and $RE_{imag}$ of different orientation defects reconstructed by $L_1$ and $L_2$ regularization method

100 kHz but smaller than that at 500 kHz. This is because the excitation currents are 0.81 A at 100 kHz and 0.27 A at 500 kHz which is larger and smaller than 0.4 A of simulation, respectively.

By comparing the voltages after normalization, the trend of voltage changes is relatively consistent between simulation and experiment. The relative error and correlation coefficient are 5.36% and 0.9996 at 100 kHz, and 8.06% and 0.9983 at 500 kHz. This indicates that the results in experiment are in accordance with simulation, which also lays the foundation of imaging in experiment reconstructed by the sensitivity calculated by simulation.

### 5.2 Forward Problem Linearization Analysis Based on Sensitivity Matrix

Table 4 and Table 5 show the $RE_{linear}$ and $CC_{linear}$ of forward problem linearization based on different initial conductivity estimate sensitivity matrices at 100 kHz and 500 kHz in experiment, respectively. Compared with the sensitivity matrix calculated with unit conductivity initial estimate, $RE_{linear}$ and $CC_{linear}$ of the high conductivity initial estimate are all improved both at 100 kHz and 500 kHz. Compared with the high conductivity initial estimate at 100 kHz, $RE_{linear}$ and $CC_{linear}$ are better at 500 kHz. The results indicate that ECT forward problem linearization is more accurate and more reliable for the sensitivity matrix calculated with high conductivity initial estimate at higher frequency. This is consistent with the simulation results as shown in Fig. 7.

### 5.3 Image Reconstruction

The defect images reconstructed by $L_1$ and $L_2$ regularization method at 100 kHz and 500 kHz with high conductivity initial estimate sensitivity matrix are shown in Fig. 15. Both $L_1$ and $L_2$ regularization method reconstruct the correct position of the defect. The defect size reconstructed by $L_2$ regularization method is larger than $L_1$ regularization method. But the shapes of the defects all fails to be reconstructed. There are many artifacts in the images reconstructed by $L_2$ regularization method, especially for defect 2' and 3' at 500 kHz.

The imaging parameters at 100 kHz and 500 kHz are shown in Table 6 and Table 7, respectively. Compared with $L_2$ regularization method, the $CC_{imag}$ and $RE_{imag}$ of $L_1$ regularization method are improved at all frequencies. For $L_1$ regularization method, the imaging parameters at 500 kHz are better than those at 100 kHz. The results of image reconstruction indicate that the $L_1$ regularization method at higher frequency of 500 kHz gets better imaging performance. This is also consistent with the simulation results.

## 6 Conclusion

For the image reconstruction of defect on high conductivity metal by ECT at higher frequency, the sensitivity matrix calculated with high conductivity initial estimate was proposed. The reliability of ECT forward problem linearization was analyzed with unit conductivity and high conductivity initial estimate by simulation and experiment. $RE_{linear}$ and $CC_{linear}$ are improved a lot with high conductivity initial estimate especially with frequency increases. This concludes that the high conductivity initial estimate sensitivity matrix makes the linearization of ECT forward problem more accurate and more reliable at higher frequency.

Two typical regularization methods (L1 and L2) were studied and compared with high conductivity initial estimate sensitivity matrix by simulation and experiment. The positions of all the defects were well located by both two imaging methods, but the size of the defects reconstructed by $L_2$ regularization method was larger than real defects while it was opposite for $L_1$ regularization method. And the imaging parameters $CC_{imag}$ and $RE_{imag}$ of $L_1$ regularization method are all better than $L_2$ especially at higher frequency. Therefore, $L_1$ regularization method was more suitable to reconstruct small defects of metal materials theoretically relative to $L_2$ regularization method, because there

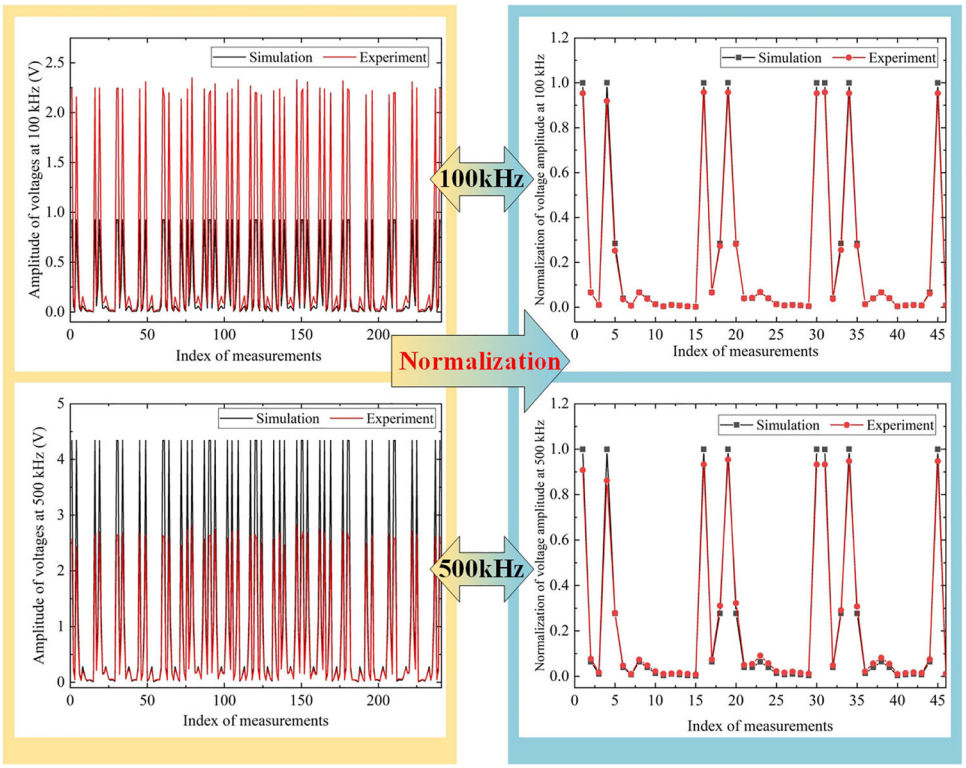


**Fig. 14** Detection voltages of simulation and experiment

**Table 4** Indicators of ECT forward problem linearization based on different initial conductivity estimate sensitivity matrices at 100 kHz in experiment

| Indicators | Initial estimate | Defect 1' | Defect 2' | Defect 3' |
|---|---|---|---|---|
| $RE_{linear}$ | High conductivity | 43% | 56% | 60% |
| | Unit conductivity | 53% | 60% | 61% |
| $CC_{linear}$ | High conductivity | 0.93 | 0.86 | 0.83 |
| | Unit conductivity | 0.84 | 0.74 | 0.74 |

**Table 5** Indicators of ECT forward problem linearization based on different initial conductivity estimate sensitivity matrices at 500 kHz in experiment

| Indicators | Initial estimate | Defect 1' | Defect 2' | Defect 3' |
|---|---|---|---|---|
| $RE_{linear}$ | High conductivity | 32% | 47% | 42% |
| | Unit conductivity | 55% | 66% | 65% |
| $CC_{linear}$ | High conductivity | 0.96 | 0.89 | 0.91 |
| | Unit conductivity | 0.84 | 0.73 | 0.67 |

are few non-zero reconstruction elements in $L_1$ prior knowledge.

There are still more works that should be done in the future, such as the shape reconstruction of defects, defect reconstruction on curved blade, improvement of coil consistency and data acquisition in experiment. This work helps to improve the metal defect image accuracy of ECT through high conductivity initial estimate sensitivity matrix at high frequency with $L_1$ regularization method. And it also expands the original assumption of ECT forward problem linearization that there is a small conductivity change between the defect state and non-defect state, to a high conductivity change with a small volume perturbation between the two states.

**Table 6** The imaging parameters reconstructed by $L_1$ and $L_2$ regularization method at 100 kHz in experiment

| Parameters | Imaging method | Defect 1' | Defect 2' | Defect 3' |
|---|---|---|---|---|
| $RE_{imag}$ | $L_2$ regularization | 143% | 128% | 132% |
| | $L_1$ regularization | 108% | 94% | 102% |
| $CC_{imag}$ | $L_2$ regularization | 0.27 | 0.22 | 0.36 |
| | $L_1$ regularization | 0.15 | 0.35 | 0.36 |

**Table 7** The imaging parameters reconstructed by $L_1$ and $L_2$ regularization method at 500 kHz in experiment

| Parameters | Imaging method | Defect 1' | Defect 2' | Defect 3' |
|---|---|---|---|---|
| $RE_{imag}$ | $L_2$ regularization | 107% | 165% | 192% |
| | $L_1$ regularization | 91% | 89% | 96% |
| $CC_{imag}$ | $L_2$ regularization | 0.42 | 0.21 | 0.31 |
| | $L_1$ regularization | 0.42 | 0.47 | 0.41 |

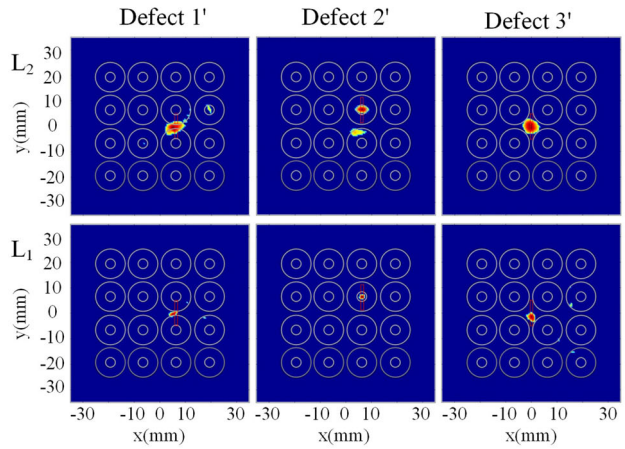


(a)

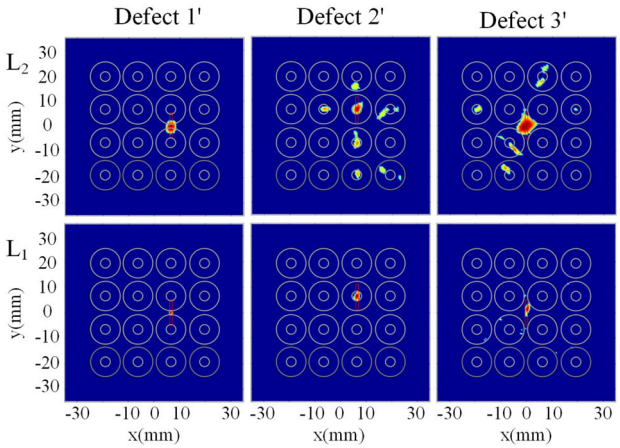


(b)

**Fig. 15** Defect images reconstructed by $L_1$ and $L_2$ regularization method with high conductivity initial estimate in experiment. (a) 100 kHz. (b) 500 kHz

**Acknowledgements** Funding that provided financial support for this article is gratefully acknowledged.

**Author Contributions** Zhili Xiao: Conceptualization, Methodology, Formal analysis, Writing - Original draft preparation, Writing - Review Editing. Zicheng Ma: Investigation. Xiaohui Li: Data curation. Chao Tan: Supervision, Writing- Reviewing and Editing. Feng Dong: Supervision, Writing- Reviewing and Editing.

**Funding** This work was supported by the National Natural Science Foundation of China (Grant number 62003353); and the Fundamental Research Funds for Central Universities, Civil Aviation University of China (Tianjin) (Grant number 3122019040).

**Availability of Data and Materials** The datasets generated or analyzed during this study are available from the corresponding author on reasonable request.

## Declarations

**Conflict of interest** The authors declare that they have no known competing financial interests or personal relationships that could have appeared to influence the work reported in this paper.

**Ethics Approval and Consent to Participate** Not applicable.

**Consent for Publication** Not applicable.

**Code Availability** The code used in this study are available from the corresponding author on reasonable request.

## References

1. Yu, X., Zhang, W., Qiu, Z., Chen, G., Qin, F.: Differential excitation eddy current sensor testing for aircraft engine blades defect. J. B. Univ. Aeronaut. Astronaut. 41(9), 1582–1588 (2015) https://doi.org/10.13700/j.bh.1001-5965.2014.0639
2. Su, Z., Ventre, S., Udpa, L., Tamburrino, A.: Monotonicity based imaging method for time-domain eddy current problems. Inverse Probl. **33**(12), 125007 (2017). https://doi.org/10.1088/1361-6420/aa909a

3. Wang, R., Bao, B., Wang, W., Zhang, M., Liu, L., Song, K.a.: Research on remote-field eddy current focusing method for detecting hidden defects in aircraft riveted components. J. Nonestruct. Eval. **42**(4), 95 (2023) https://doi.org/10.1007/s10921-023-01011-2
4. Xiao, Z., Li, X., Ma, Z.: Crack locating in high conductivity plate based on planar array pect. In: 2023 42st Chinese Control Conference (CCC), pp. 3199–3204 (2023). https://doi.org/10.23919/CCC58697.2023.10240729
5. Huang, P., Li, Z., Pu, H., Jia, J., Liu, K., Xu, L., Xie, Y.: Conductivity measurement of non-magnetic material using the phase feature of eddy current testing. J. Nonestruct. Eval. **42**(2), 50 (2023). https://doi.org/10.1007/s10921-023-00958-6
6. Ricci, M., Silipigni, G., Ferrigno, L., Laracca, M., Adewale, I.D., Tian, G.Y.: Evaluation of the lift-off robustness of eddy current imaging techniques. NDT & E Int. **85**, 43–52 (2017). https://doi.org/10.1016/j.ndteint.2016.10.001
7. Wang, Y., Niu, Y., Wei, Y., Ye, C.: Multi-frequency imaging with non-linear calibration of magnetoresistance sensors for surface and buried defects inspection. NDT & E Int. **132**, (2022) https://doi.org/10.1016/j.ndteint.2022.102706
8. Park, J.W., Lee, T.G., Back, I.C., Park, S.J., Seo, J.M., Choi, W.J., Kwon, S.G.: Rail surface defect detection and analysis using multi-channel eddy current method based algorithm for defect evaluation. J. Nonestruct. Eval. **40**(3), 83 (2021). https://doi.org/10.1007/s10921-021-00810-9
9. Rubinacci, G., Tamburrino, A., Ventre, S.: Regularization and numerical optimization of a fast eddy current imaging method. IEEE Trans. Mag. **42**(4), 1179–1182 (2006). https://doi.org/10.1109/TMAG.2006.872477
10. Tamburrino, A., Calvano, F., Ventre, S., Rubinacci, G.: Non-iterative imaging method for experimental data inversion in eddy current tomography. NDT & E Int. **47**, 26–34 (2012). https://doi.org/10.1016/j.ndteint.2011.11.013
11. Nowak, P., Szewczyk, R., Ostaszewska-Lizewska, A.: Inverse transformation in eddy current tomography with continuous optimization of reference defect parameters. Materials **14**(17), (2021) https://doi.org/10.3390/ma14174778
12. He, D.F., Shiwa, M., Jia, J.P., Takatsubo, J., Moriya, S.: Multi-frequency ECT with AMR sensor. NDT & E Int. **44**(5), 438–441 (2011). https://doi.org/10.1016/j.ndteint.2011.04.004
13. Premel, D., Mohammad-Djafari, A.: Eddy current tomography in cylindrical geometry. IEEE Trans. Mag. **31**(3), 2000–2003 (1995). https://doi.org/10.1109/20.376435
14. Griffiths, H.: Magnetic induction tomography. Meas. Sci. Technol. **12**(8), 1126–1131 (2001). https://doi.org/10.1088/0957-0233/12/8/319
15. Zaoui, A., Menana, H., Feliachi, M., Abdellah, M.: Generalization of the ideal crack model for an arrayed eddy current sensor. IEEE Trans. Mag. **44**(6), 1638–1641 (2008). https://doi.org/10.1109/TMAG.2007.914846
16. Zaoui, A., Menana, H., Feliachi, M., Berthiau, G.: Inverse problem in nondestructive testing using arrayed eddy current sensors. Sensors **10**(9), 8696–8704 (2010). https://doi.org/10.3390/s100908696
17. Dingley, G., Soleimani, M.: Multi-frequency magnetic induction tomography system and algorithm for imaging metallic objects. Sensors **21**(11), (2021) https://doi.org/10.3390/s21113671
18. Merwa, R., Hollaus, K., Brunner, P., Scharfetter, H.: Solution of the inverse problem of magnetic induction tomography (MIT). Physiol. Meas. **26**(2, SI), 241–250 (2005) https://doi.org/10.1088/0967-3334/26/2/023
19. Soleimani, M., Lionheart, W.R.B.: Absolute conductivity reconstruction in magnetic induction tomography using a nonlinear method. IEEE T. Med. Imaging **25**(12), 1521–1530 (2006). https://doi.org/10.1109/TMI.2006.884196
20. Zolgharni, M., Griffiths, H., Ledger, P.D.: Frequency-difference MIT imaging of cerebral haemorrhage with a hemispherical coil array: numerical modelling. Physiol. Meas. **31**(8, SI), 111–125 (2010) https://doi.org/10.1088/0967-3334/31/8/S09
21. Ma, L., Wei, H.-Y., Soleimani, M.: Planar magnetic induction tomography for 3D near subsurface imaging. Prog. Electromagn. Res. **138**, 65–82 (2013). https://doi.org/10.2528/PIER12110711
22. Yin, W., Peyton, A.J.: A planar emt system for the detection of faults on thin metallic plates. Meas. Sci. Technol. **17**(8), 2130–2135 (2006). https://doi.org/10.1088/0957-0233/17/8/011
23. Hollaus, K., Magele, C., Merwa, R., Scharfetter, H.: Fast calculation of the sensitivity matrix in magnetic induction tomography by tetrahedral edge finite elements and the reciprocity theorem. Physiol. Meas. **25**(1), 159–168 (2004). https://doi.org/10.1088/0967-3334/25/1/023
24. Xiao, Z., Tan, C., Dong, F.: 3-D hemorrhage imaging by cambered magnetic induction tomography. IEEE Trans. Instrum. Meas. **68**(7), 2460–2468 (2019). https://doi.org/10.1109/TIM.2019.2900779
25. Chen, Y., Dong, F., Tan, C.: Space-constrained optimized tikhonov regularization method for 3d hemorrhage reconstruction by open magnetic induction tomography. Phys. Med. Biol. **67**(22) (2022) https://doi.org/10.1088/1361-6560/ac9e42
26. Zolgharni, M.: Magnetic induction tomography for imaging cerebral stroke. PhD thesis, Swansea University (2010)
27. Auld, B.A., Moulder, J.C.: Review of advances in quantitative eddy current nondestructive evaluation. J. Nonestruct. Eval. **18**(1), 3–36 (1999). https://doi.org/10.1023/A:1021898520626
28. Chen, Y., Tan, C., Dong, F.: Combined planar magnetic induction tomography for local detection of intracranial hemorrhage. IEEE Trans. Instrum. Meas. **70**, (2021) https://doi.org/10.1109/TIM.2020.3011621
29. Ktistis, C., Armitage, D.W., Peyton, A.J.: Calculation of the forward problem for absolute image reconstruction in mit. Physiol. Meas. **29**(6, SI), 455–464 (2008) https://doi.org/10.1088/0967-3334/29/6/S38
30. Korjenevsky, A.V., Cherepenin, V.A.: Progress in realization of magnetic induction tomography. Ann. NY Acad. Sci. **873**, 346–352 (1999). https://doi.org/10.1111/j.1749-6632.1999.tb09482.x
31. Xiao, Z., Tan, C., Dong, F.: Effect of inter-tissue inductive coupling on multi-frequency imaging of intracranial hemorrhage by magnetic induction tomography. Meas. Sci. Technol. **28**(8), (2017) https://doi.org/10.1088/1361-6501/aa7504
32. Xiao, Z., Ma, Z.: Upper limit frequency analysis of eddy current testing for high conductive plate. In: 2022 41st Chinese Control Conference (CCC), pp. 3020–3025 (2022). https://doi.org/10.23919/CCC55666.2022.9902837
33. Liu, X., Liu, Z.: A novel algorithm based on $L_1$-$L_p$ norm for inverse problem of electromagnetic tomography. Flow Meas. Instrum. **65**, 318–326 (2019). https://doi.org/10.1016/j.flowmeasinst.2019.01.010
34. Stephen, B., Lieven, V.: Convex Optimization, pp. 305–317. Cambridge University Press (2004)


**Publisher's Note** Springer Nature remains neutral with regard to jurisdictional claims in published maps and institutional affiliations.

Springer Nature or its licensor (e.g. a society or other partner) holds exclusive rights to this article under a publishing agreement with the author(s) or other rightsholder(s); author self-archiving of the accepted manuscript version of this article is solely governed by the terms of such publishing agreement and applicable law.